Enhancing the degradation efficiency of OPs under visible light by an integrated cascade photo-biocatalyst

Ying Zhang[1‡], Xue Cao[1‡], Xiaotian Wang[1], Lihui Wang[1], Sumin Guan[1], Heyu Li[2], Xiaobing Zheng[1, 3]*, Yanjun Jiang[1, 4]*, Jing Gao[1]

[1] School of Chemical Engineering and Technology, Hebei University of Technology, 8 Guangrong Road, Hongqiao District, Tianjin, 300130, China.

[2] Tianjin UBasio Biotechnology Group Co., LTD., 276 Huanghai Road, TEDA, TianJin, 300457, China.

[3] National Local Joint Engineering Laboratory for Energy Conservation of Chemical Process Integration and Resources Utilization, Hebei University of Technology, Tianjin 300130, China.

[4] Tianjin Key Laboratory of Chemical Process Safety, Hebei University of Technology, 8 Guangrong Road, Hongqiao District, Tianjin 300130, China

[‡] Ying Zhang and Xue Cao contributed equally

***Corresponding author:**

Xiaobing Zheng and Yanjun Jiang

School of Chemical Engineering and Technology, Hebei University of Technology, 8 Guangrong Road, Hongqiao District, Tianjin, 300130, China

Phone/fax: +8613512901656 and +8613752061144

E-mail: zhengxiaobing@hebut.edu.cn and yanjunjiang@hebut.edu.cn

Funding information

This work was supported by the National Natural Science Foundation of China

[No. 21576068, 21878066 and 21878068]; the Natural Science Foundation of Hebei Province [B2015202082 and B2017202056]; the Program for Top 100 Innovative Talents in Colleges and Universities of Hebei Province [SLRC2017029] and Hebei High Level Personnel of Support Program [A2016002027]; National College Student's Science and Technology Innovation Project [202010080038].

Abstract: Photo-enzymatic integrated nanocatalyst which combined biocompatible photocatalytic carrier and OPH is designed to remove OPs. H-TiO_2 microsphere is prepared using wrinkled SiO_2 as template. Then, Au nanoparticles are loaded on the H-TiO_2 to obtain Au-H-TiO_2 heterojunction microsphere, which achieved effective use of visible light based on the SPR. The characterization results of Au-H-TiO_2 prove that the Au-H-TiO_2 has large specific surface area (226.19 m^2/g) and narrow band gap (2.68 eV). Adsorption methods are used to prepare OPH@Au-H-TiO_2 by immobilizing OPH molecules. The obtained OPH@Au-H-TiO_2 can degrade methyl parathion to p-NP by OPH. Then the p-NP is degraded to hydroquinone with low toxicity using Au-H-TiO_2. After 2.5 h, methyl parathion is completely degraded, and about 82.64% of the generated p-NP is further degraded into hydroquinone. The fabricated OPH@Au-H-TiO_2 has excellent catalytic activity and cycle stability, which is ascribed to the photo-enzyme synergic catalytic effect.

KEYWORDS
photo-enzyme integrated catalyst, heterojunction, immobilized enzyme, visible light, cascade catalysis

1 Introduction

Pesticides are widely used in agriculture due to their efficient and acute toxic functions, and many developing countries regard pesticides as the important tool of crop protection and adopts pesticides to improve the agricultural productivity and production efficiency [1-3]. Organophosphorus pesticides (OPs) are one kind of the widely used pesticide species, accounting for 34% of the world's pesticides use. The phosphate ester bond of OPs can inhibit the activity of acetylcholinesterase (AChE), leading to the accumulation of AChE, which has an important effect on the central nervous system of mammals and insects. Thus, OPs can achieve the goal of insecticidal extermination, so as to prevent the occurrence of agricultural pests and diseases [2]. However, residual OPs with persistence can enter the food chain through their accumulation in air, water and soil, and with the enrichment of toxic substances, which will eventually build up in consumers' bodies, leading to serious health complications [4]. Therefore, it is of great importance to eliminate pesticide residues in water.

There are chemical degradation and biodegradation methods to remove pesticide residues. At present, semiconductor-based photocatalysis is one of the most promising chemical degradation methods to solve growing issues about pesticide residues [5]. TiO_2 has been widely studied and applied thanks to its excellent photocatalytic performance, low cost and high chemical stability [6]. Up to now, TiO_2 has been widely used in the fields of degradation, water cracking and other fields [6]. However, the TiO_2-based photocatalyst face two important problems: low visible light utilization and

high carrier recombination rate [7]. In order to overcome these problems and improve the photocatalytic performance, people have worked hard to adjust the energy band [8], manufacture electron traps [9], etc.

The noble metal modification of the oxide surface, according to the role of surface plasmon resonance (SPR) and the synergistic effect of noble metal and support material, can adjust the adsorption band, thereby further improving its photocatalytic performance [10-12]. Several noble metals such as Au, Pt and Pd modify the surface of TiO_2 to achieve the photodegradation of contaminant under visible light. Therefore, the preparation of Au modified nanomaterials with special photoactivity is a hot research topic.

Besides the modification of Au on the surface of TiO_2, the hollow structure is conducive to visible light acquisition, because of the multiple scattering of light in the inner cavity, the problem of electron hole pair separation can be effectively overcome. Meanwhile, the retention time of photocatalyst can be controlled and the process path of mass transfer and charge transfer can be shortened, which contributing to its promising applications in various fields [11-12]. In addition, the larger specific surface area of hollow structure can provide more attachment sites and reaction sites. Moreover, a relatively independent microenvironment is formed in the shell, and the pore structure facilitates the passage of reactants, which is benefit for the limiting effect of catalytic reaction. Given these properties, hollow structure is ideal in designing a novel photocatalyst with improved photoactivity.

Organophosphorus hydrolase (OPH, EC 3.1.8.1), also known as

phosphotriesterase, belongs to the class of amide hydrolases, and degrades OPs mainly by breaking the P-C bond, P-O bond and P-S bond [13]. However, there are still some disadvantages of degrading OPs by using free enzymes, such as high cost, low stability, low reusability and poor tolerance of microbial degrading enzymes to harmful substances [14]. Immobilization of OPH onto mesoporous carriers may ensure their high activity and stability to reduce inhibition by product [15]. Similarly, the immobilization of OPH into hollow carrier can prevent intermolecular interactions and protect free OPH from interaction with external interfaces, thus leading to the inactivation of the enzyme due to undesired conformational changes. At the same time, the hollow structure greatly increases the amount of immobilized enzyme.

Herein, a photo-enzyme integrated catalyst (named as OPH@Au-H-TiO_2) was prepared for the degradation of methyl parathion in visible light via cascade catalytic reactions. As shown in Scheme 1, SiO_2 nanoflowers were used as the template, and TiO_2 shells with regular structure were grown on its surface. After removal the SiO_2 nanoflowers by etching, porous hollow SiO_2@TiO_2 (H-TiO_2) microspheres were obtained. Then, the etching time was adjusted to further study the effect of Si-O-Ti bond on visible light utilization and photocatalytic ability. Then, Au were well modified on the H-TiO_2 microspheres to promote visible light utilization and charge separation. Finally, OPH are immobilized on the Au-H-TiO_2 microspheres by adoption, and the photo-enzyme integrated catalyst (named as OPH@Au-H-TiO_2) was obtained. The possible synergistic catalytic mechanism of photo-enzyme integrated catalyst was discussed in detail. There are five advantages of the photo-enzyme

integrated nanocatalyst: (I) The Brönsted site is formed by incomplete etching of SiO_2, which activates the oxidation reaction [16]. (II) The O atom between Ti and Si increases the electron activation rate, thus improving the photodegradation efficiency [17-18]. (III) The Au surface plasmon resonance effect can improve the response range of the composite to visible light. (IV) Au has good biocompatibility and mechanical stability, and can interact with the groups of enzyme molecules to enhance the immobilization of enzymes [12]. (V) The photo-enzyme integrated catalyst can realize the synergistic effect under visible light. As expected, the obtained OPH@Au-H-TiO_2 shows the efficient catalytic activity and durability for removing OPs in water.

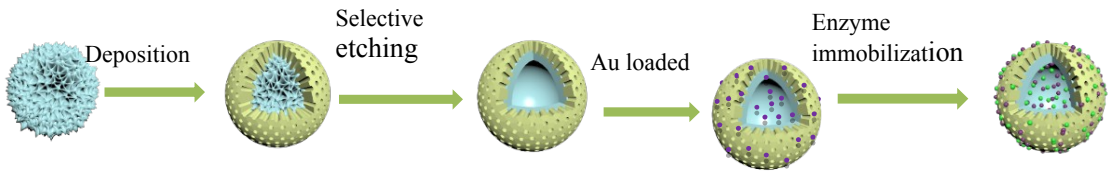

Scheme 1. Schematic illustration for the fabrication procedure of OPH@Au-H-TiO_2 composite photocatalyst

2 Material and methods

2.1 Materials

Tetraethoxysilane (TEOS) and n-butanol were purchased from Tianjin Damao Chemical Reagent Factory. Cetyl trimethyl ammonium bromide (CTAB) and urea were purchased from Aladdin. Cyclohexane, ammonia water and anhydrous ethanol were purchased from Tianjin Fengchuan Chemical Reagent Technologies Co., Ltd. Tetrabutyl titanate (TBOT) was purchased from Tianjin Kermel Chemical Reagent Technologies Co., Ltd. Organophosphorus hydrolase (OPH, EC 3.1.8.1) was

purchased from Beijing Schengenbiya Biotechnology Co., Ltd. P-nitrophenol (P-NP) was purchased from Chengdu Aikeda Chemical Reagent Co., Ltd. Parathion-methyl was purchased from Dr. Ehrenstorfer.

2.2 Preparation of catalysts

2.2.1 Synthesis of H-TiO_2

SiO_2 nanoflowers were synthesized according to the previous reported method [19]. Then, 0.15g of SiO_2 nanoflowers were dissolved in 200 mL of anhydrous ethanol, and 0.9 mL of ammonia water (25% wt) was added and mixed with ultrasound for 15 min to form a transparent solution. Subsequently, 2 mL of TBOT was added dropwise and stirred uniformly for 24 h at 45°C. The reaction product was washed for several times, then centrifuged and dried. After drying, the product was calcined in air in a tubular furnace at the rate of 1°C/min heated to 450°C and kept for 1 h. The obtained SiO_2@TiO_2 samples were dispersed into 6 M ammonia water and stirred evenly at 80°C for 8 h. The resulting product was washed for several times, then centrifuged and dried to obtain hollow TiO_2 (H-TiO_2).

2.2.2 Synthesis of Au-H-TiO_2

0.10 g of H-TiO_2 was dissolved in 5 mL water and mixed with ultrasound for 15 min. After dispersing evenly, 5 mL $HAuCl_4$ (1, 2 and 4 mg/mL) was added and stirred at room temperature for 4 h. Then, 5 mL $NaBH_4$ (100 mM) was slowly added and stirred for 2 h to obtain purple-black products. The obtained product was washed for several times and vacuum dried, then Au-H-TiO_2 was obtained.

2.3 Preparation of photo-enzyme integrated catalyst OPH@Au-H-TiO_2 and assaying the enzyme activity

30 mg of Au-H-TiO_2 was dispersed in 15 mL Tris-HCl buffer solution (pH 8), containing different concentrations OPH (4, 6, 8 and 10 mg/mL). The mixture was placed in an incubator with 170 rpm at 25°C for shaking 90 min to reach adsorption equilibrium. The immobilized OPH on Au-H-TiO_2 was separated by centrifugation and washed with Tris-HCl buffer solution, and the obtained solid product was OPH@Au-H-TiO_2. Bradford method was used to assess enzyme loading on the OPH@Au-H-TiO_2. The specific activity was assayed by using methyl parathion (30 μmol/mL in water) as the substrate. Typically, 0.1 mL of methy-parathion solution was added to the solution containing the OPH@Au-H-TiO_2 (30 mg). After reaction for 3 min, the concentration of the produced p-nitrophenol (p-NP) was detected by absorbance at 410 nm on a spectrophotometer. One unit of specific activity was defined as the amount of OPH@Au-H-TiO_2 needed to release 1 μmol of p-NP per minute.

2.4 Characterization

The morphology of catalysts was observed by scanning electron microscopy (SEM, FEI NanoSEM450 microscope under 5 KV accelerating voltages). The internal structures of catalysts were observed with a transmission electron microscope (TEM and HRTEM, JEOL-2100F under 4300V accelerating voltages). X-ray powder diffractometer (XRD) on Bruker AXS D8 was used to detect the crystal structure of

the catalysts. X-ray photoelectron spectroscopy (XPS, Thermo Scientific K-Alpha) was acquired to examine the element composition, chemical states and valance state of the samples. Confocal laser scanning microscopy (CLSM) was used to detect the distribution of OPH with a Leica TCS SP5 confocal microscope. The Fourier transform infrared (FTIR) of the catalysts were performed with a Bruker, VECTOR22 spectrometer. Ultraviolet visible diffuse reflectance spectra (UV-DRS) were measured on a U-3010 spectrophotometer (Hitachi, Japan) UV-Vis spectrophotometer. The samples were also analyzed by using electron paramagnetic resonance photoluminescence (PL) spectra (Fluorolog3-21 from Jobin Yvon). The Brunauer-Emmett-Teller (BET) surface area and Barrett–Joyner–Halenda (BJH) pore size distribution were determined by Micromeritics ASAP 2020 system at 77 K.

2.5 Application of OPH@Au-H-TiO_2 in degrading organophosphorus pesticides

2.5.1 Determination of degradation rate of methyl parathion

As shown in Scheme 2, in the Model 1, the cascade reaction is conducted stepwise. In this model, the reaction can be divided into two steps: enzyme catalysis and photocatalysis. The OPH@Au-H-TiO_2 was firstly placed in the dark and stirred magnetically at 40°C for 1.5 h to degrade OPs by OPH. Then the solution was transferred to visible light and the produced p-NP can be degraded by Au-H-TiO_2 under visible light excitation. For comparison, OPH@Au-H-TiO_2 was directly placed under visible light at a constant temperature for 1.5 h to degrade OPs by OPH@Au-H-

TiO_2 under visible light excitation (Model 2), where the enzymatic catalysis and photocatalysis were conducted simultaneously. Under Model 1 and Model 2, 30 mg of OPH@Au-H-TiO_2 was dispersed in 9.9 mL water and then 0.1 mL methyl parathion (30 μmol/mL) was added. Then, 1 mL suspension was taken out at given time intervals, centrifuged, and the supernatants were taken out. The concentration of methyl parathion and content of p-NP were respectively measured for the absorption value of supernatant at 275 nm and 315 nm.

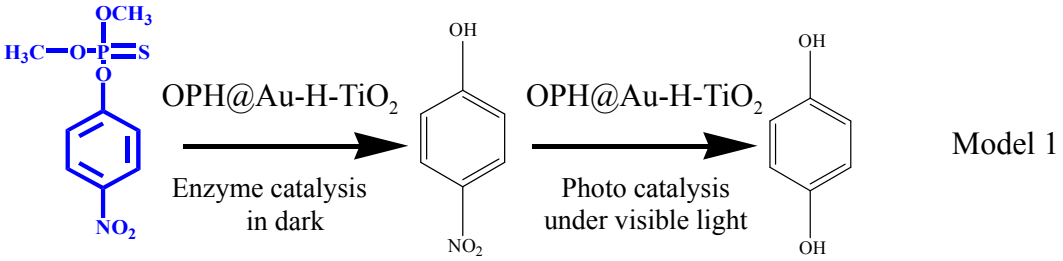

Model 1

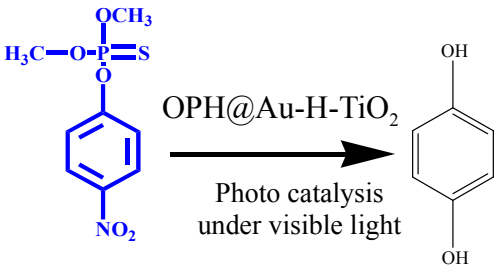

Model 2

Scheme 2. Proposed different modes of methyl parathion degradation

2.5.2 Evaluation of the reactive oxidizing species

To further confirm the active species that play a major role in the photocatalytic oxidative degradation of p-NP. Benzoquinone (BQ), isopropanol (IPA) and ethylene diamine tetracetic acid-2Na (EDTA-2Na) were used to eliminate $\bullet O_2^-$, •OH and h^+ respectively for the scavenger collection experiments [20]. Firstly, 30 mg of the

OPH@Au-H-TiO_2 were added into 10 mLp-NP (10 mg/mL) solution and stirred for 0.5 h in the dark. After that, BQ (1 mmol/L), IPA (1:15V/V) and EDTA-2Na (10 mmol/L) were added into the mixture and illuminated under Xe-lamp (500 W) with continuous stirring. Then, the suspension was collected, centrifuged, and analyzed at 315 nm by an UV-vis spectrophotometer.

2.5.3 Reusability of the OPH@Au-H-TiO_2

Reusability of OPH@Au-H-TiO_2 is assessed by degrading methyl parathion. Typically, 30 mg of OPH@Au-H-TiO_2 was added to 9.9 mL water and dispersed evenly. Then 0.1 mL 30 μmol/mL methyl parathion was added. After reaction, the supernatant was removed by centrifugation and the absorption values of the supernatant at 275 nm were measured. Subsequently, it was reused in a new reaction mixture.

3 Results and discussion

3.1 Preparation of H-TiO_2

The surface morphology and internal structure of SiO_2 nanoflowers are investigated by SEM and TEM respectively. From Fig. S1a, SiO_2 nanoflowers are highly dispersed and uniform spherical nanoparticles with particle size of about 350 nm and an obvious mesoporous structure on the external surface [19]. As can be seen from Fig. S1b, SiO_2 nanoflowers are the fibrous bundle structures, and the structures can effectively increase the specific surface area [21].

According to the Fig. 1a, Ti element is evenly distributed in the spherical shell,

while Si element is evenly distributed in the spherical core position. Fig. 1b is the obtained TiO_2 with hollow structure (H-TiO_2), and surface defects of the hollow structure can be observed from SEM and TEM diagrams. From the qualitative distribution of the elements in the mapping image, the Si and O elements of the core position are significantly reduced compared with SiO_2@TiO_2, and the distribution of Ti element remains the same, indicating that SiO_2 is partially etched to form a hollow structure [22-23]. The partial etching of Si element makes the refraction occurs from TiO_2 to SiO_2 and then into the cavity, which increases the refraction path and thus improves the photocatalytic activity. The hollow structure is advantageous to the use of light in photocatalysis.

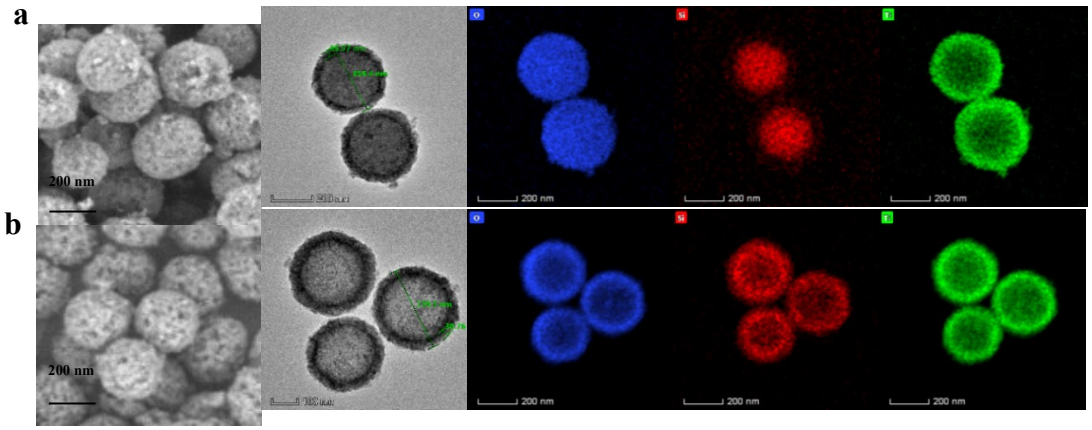

Fig. 1 SEM, TEM and Mapping images of SiO_2@TiO_2 and H-TiO_2.

Crystal phase and crystallinity are two important factors affecting photocatalysis. The separation and transfer rate of electrons from holes depend on the increase of crystallinity. Moreover, the photocatalytic efficiency of anatase is better than that of rutile and brookite. Some studies showed that the Ti-O-Si bond can inhibit TiO_2 nucleation, thus affecting the change of crystal phase. Therefore, the effect of etching degree on the crystal phase and crystallinity of H-TiO_2 was studied by changing etching time. Fig. 2 shows the XRD patterns of different etching time of H-TiO_2. Peaks around 25.4°, 37.9°, 48.0°, 53.8°, 54.9° and 62.8° correspond to the crystal

surfaces of anatase TiO_2 (101), (004), (200), (105), (211), (204), which are consistent with anatase TiO_2 (JCPDS No.21-1272) [24], and sharp peak pattern confirmed that H-TiO_2 have good crystallization. This is because the Ti-O-Si bonds in H-TiO_2 will inhibit the growth of particles, thus stabilizing anatase crystal phase. In addition, some Ti atoms will replace Si atoms of tetragonal coordination, and the interaction between Ti atoms of tetragonal coordination and Ti atoms of octet coordination will inhibit the formation of rutile phase [25]. However, H-TiO_2 display amorphous with the extension of time, which may be due to the Oswald ripening effect [26-28]. The number of free atoms in the solvent will increase due to the dissolution of SiO_2. When the free atoms in the reaction system reach the supersaturated state, they will deposit on the surface of TiO_2, presenting as SiO_2 amorphous peak. TEM patterns of different etching time of H-TiO_2 (Fig. S2) and EDS (Table. S1) are also confirmed this result. When the etching time is 8 h, the hollow structure is more complete, and the surface area is the largest. According to the above results, the etching time of 8 h is selected for subsequent experiments.

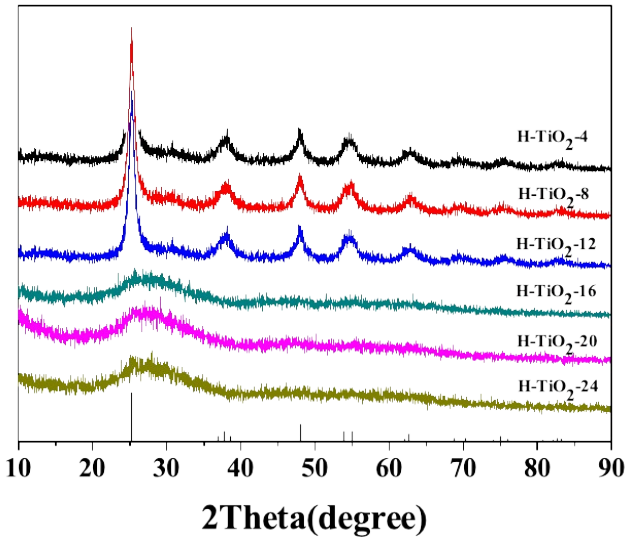

Fig. 2 XRD patterns of different etching time of H-TiO_2

3.2 Characterization of Au-H-TiO_2

The elements distribution in Fig. S3 shows that Au element uniformly distributed

on the H-TiO_2 sphere, indicating that Au is successfully loaded on the H-TiO_2 and Au-H-TiO_2 is obtained. According to the HRTEM image in Fig. S3, the uniform distribution of Au nanoparticles and two kinds of clear lattice fringes are observed, and the lattice spacing of 0.23 nm and 0.35 nm correspond to the Au (111) and TiO_2 anatase phase (101) crystal plane respectively [29]. These results prove the fine crystallinity and heterojunction structure formed by Au and H-TiO_2 microspheres.

The BET surface area and the BJH pore size distributions of obtained SiO_2 nanoflowers, SiO_2@TiO_2, H-TiO_2 and Au-H-TiO_2 are investigated by N_2 adsorption-desorption isotherms. From Fig. 3 and Table. S2, all the materials show characteristic type IV isotherms with a H3-type hysteresis loop [30], indicating the existence of mesopores. SiO_2 nanoflowers exhibit the largest specific surface area, which is related to its fibrous structure. The specific surface area of Au-H-TiO_2 decrease from 405.34 m^2/g to 226.19 m^2/g compared to SiO_2 nanoflowers, which is because that the fiber bundle structure is disappeared after coating TiO_2 onto the SiO_2 surface. According to the Fig. 4b, the pore size of Au-H-TiO_2 is expanded to 11.70 nm from 6.25 nm due to the hollow structure formed by the dissolved part of SiO_2. These results indicate that Au-H-TiO_2 has a relatively higher specific surface area and larger pore size.

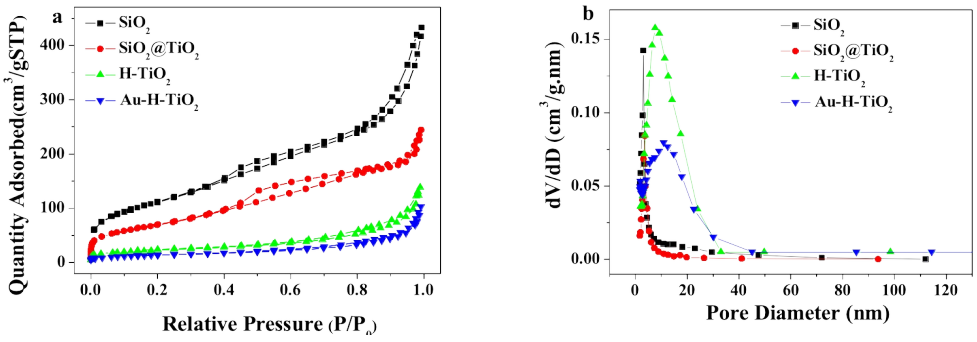

Fig. 3 Nitrogen absorption-desorption isotherms (a) and Barrett–Joyner–Halenda (BJH) pore size distribution (b) of SiO_2, SiO_2@TiO_2, H-TiO_2 and Au-H-TiO_2.

Fig. S4 shows the XRD image of the SiO_2 nanoflowers, SiO_2@TiO_2, H-TiO_2 and Au-H-TiO_2. The diffraction peak of pure SiO_2 appears at 20°. The sharp and high peaks of SiO_2@TiO_2, H-TiO_2 and Au-H-TiO_2 XRD patterns indicated that these materials have higher crystallinity. In addition, it is difficult to distinguish the diffraction peak of Au due to the small loading amount of Au and the coincidence of Au diffraction peak at 38.1° and TiO_2 diffraction peak at 37.9°.

The light absorption range of H-TiO_2 and Au-H-TiO_2 were analyzed by DRS respectively. From Fig. 4a, compared to H-TiO_2, the Au-modified Au-H-TiO_2 significantly enhance visible light absorption capacity, which can increase the range of light absorption band. This result can be put down to the formation of Schottky junction between H-TiO_2 and Au nanoparticles, which facilitates the separation of photogenerated charges. Besides, SPR of Au nanoparticles loaded on H-TiO_2 can inhibit the recombination electron hole pairs and thus increase the light absorption in the visible light range [31-34]. According to the Tauc curve in Fig. 4b, the band gap width of H-TiO_2, Au-1-H-TiO_2, Au-2-H-TiO_2 and Au-4-H-TiO_2 is 2.97 eV, 2.84 eV, 2.70 eV and 2.68 eV respectively by Kubelka-Munk transformation. With the increase of Au content, the absorption of visible light increases and the band gap width decrease, which is conducive to the absorption and utilization of light in visible light.

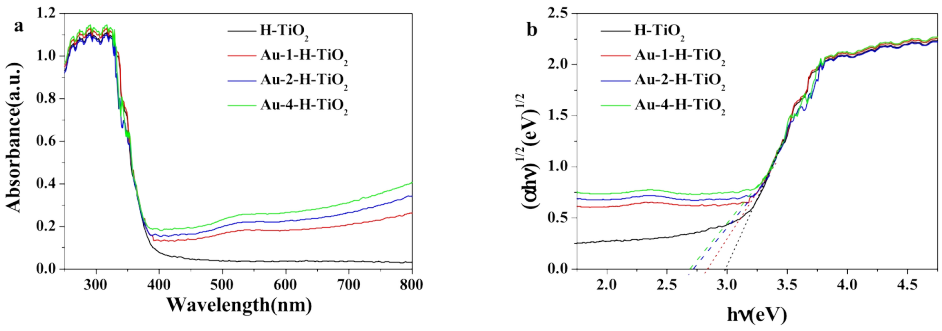

Fig. 4 (a) UV-vis diffuse reflectance spectra of H-TiO_2, Au-1-H-TiO_2, Au-2-H-TiO_2 and Au-4-H-TiO_2 and (b) their corresponding plots of (αhν)1/2 versus energy (hν).

The photoluminescence spectra are employed to reveal the separation capability of photoelectron-hole pairs of the H-TiO_2 and Au-H-TiO_2 at 304 nm excitation wavelength. From Fig. 5, the emission peak of H-TiO_2 near 475 nm is the strongest, indicating that the photogenerated carrier recombination rate is high [35]. Compared with H-TiO_2, the peak strength of Au-H-TiO_2 is significantly reduced, indicating that Au nanoparticles can effectively inhibit the photoelectron-hole pairs recombination, thus accelerate the photocatalytic rate of Au-H-TiO_2.

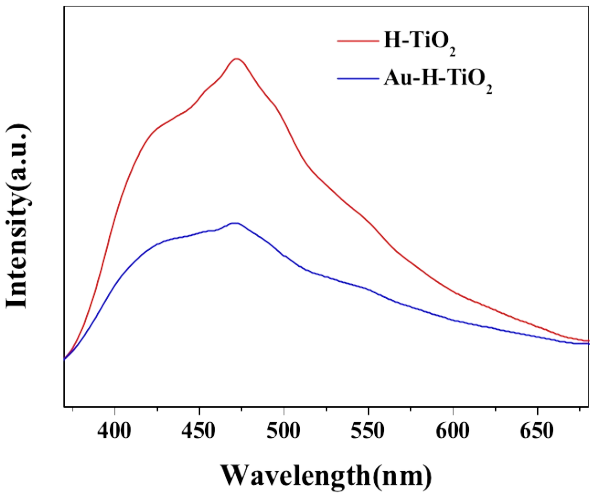

Fig. 5 PL spectra of H-TiO_2 and Au-H-TiO_2.

3.3 Preparation and Characterization of OPH@Au-H-TiO_2

To confirm the successful immobilization of OPH on Au-H-TiO_2, energy

dispersive spectrometer (EDS) mapping and confocal laser scanning microscopy (CLSM) of OPH@Au-H-TiO_2 are studied. According to TEM-mapping images of OPH@Au-H-TiO_2 (Fig. S5), N element is evenly distributed on the Au-H-TiO_2 carrier, manifesting that the OPH enzyme molecules is successfully immobilized on the Au-H-TiO_2. To get more intuitive information, fluorescently labeled OPH (FITC labeled OPH) molecules is also immobilized on the Au-H-TiO_2. According to Fig. S6, the green dots confirm the successful immobilization of OPH on Au-H-TiO_2.

Fourier transform infrared spectroscopy (FTIR) is conducted to study the functional group composition of Au-H-TiO_2 and OPH@Au-H-TiO_2 carrier. The analysis results are shown in Fig. S7, by comparing the FTIR spectra of SiO_2, H-TiO_2, Au-H-TiO_2 and OPH@Au-H-TiO_2, it is found that the wide band at 3430 cm^{-1} corresponds to the stretching vibration of hydroxylation [36]. The peak at 806 cm^{-1} is the antisymmetric telescopic absorption peak of Si-O-Si [37]. H-TiO_2, Au-H-TiO_2 and OPH@Au-H-TiO_2 show characteristic peaks at 500 cm^{-1}, 1080 cm^{-1} and 950 cm^{-1}, which ascribe the stretching vibration of Ti-O, Si-O-Si and Ti-O-Si respectively. Among them, the characteristic peak of OPH@Au-H-TiO_2 at 1549 cm^{-1} corresponds to the amide II band [38], confirming that the OPH is loaded successfully on Au-H-TiO_2.

To analyze the element composition and chemical state of H-TiO_2, Au-H-TiO_2 and OPH@Au-H-TiO_2. The full XPS surveys (Fig. S8a) indicate that Ti, O and Si elements exist in H-TiO_2, and N and Au elements are detected in OPH@Au-H-TiO_2 and Au-H-TiO_2 respectively. In the high-resolution spectrum of Ti 2p (Fig. S8b), the two peaks at 457.9 eV and 463.6 eV correspond to Ti 2p3/2 and Ti 2p1/2 respectively,

indicating the existence of Ti^{4+} in TiO_2 [39]. Compared with H-TiO_2, the peak position of Ti 2p in SiO_2@TiO_2 samples moves towards the direction of high binding energy, which is because that the existence of Ti-O-Si bond will reduce the charge density of Ti atoms (Fig. S8c). The high-resolution spectrum of Si 2p (Fig. S8d) is obtained with a distinct peak at 102.5 eV, which corresponds to the oxidation state of Si^{4+}. The peak position of Si 2p in SiO_2@TiO_2 and H-TiO_2 samples move towards the direction of low binding energy, which is related to the existence of TiO_2. In addition, the peak value of SiO_2@TiO_2 and H-TiO_2 decreased, because of the decrease of SiO_2 content (Fig. S8e). Similarly, the two peaks of 529.3 and 531.5 eV in the high-resolution spectrum of O 1s (Fig. S8f) are attributed to the Ti-O-Ti and Si-O-Ti bonds [40], among that the peak of 530.9 eV in OPH@Au-H-TiO_2 put down to the O in the OPH enzyme molecule. Furthermore, from the high-resolution XPS spectra of Au 4f (Fig. S8g), the two peaks at 82.4 eV and 86.1 eV represent the Au $4f_{5/2}$ and Au $4f_{7/2}$ respectively, indicating that Au is loaded on H-TiO_2 with Au^0 [41]. In addition, in Fig. S8h, the N 1s peak exists at 399.8 eV on OPH@Au-H-TiO_2, showing that the OPH enzyme is successfully loaded on the Au-H-TiO_2.

The preparation conditions of OPH@Au-H-TiO_2 photo-enzymatic integrated nanocatalyst were also optimized. As shown in Fig. 6a, as the adsorption time increases, the loading amount of OPH increases; however, when the adsorption time increase to 90 min, the loaded OPH reach the maximum. It can be seen in Fig. 6b that as the initial enzyme concentration increases, the loading amount of OPH increases. When the initial enzyme concentration is 9 mg/mL, the degradation activity of

OPH@Au-H-TiO_2 reaches the maximum of 528.49 U/$g_{support}$. At this time, the loaded protein is 160.15 mg/$g_{support}$. The reason may lie in that the attachment sites of enzyme molecules on the H-TiO_2 are limited, which reached saturation with the increase of enzyme concentration. Therefore, the optimal initial enzyme concentration is 9 mg/mL, and the optimum adsorption time is 90 min, and the recovery rate of enzyme activity is 62.50%.

The catalytic activity of OPH@Au-H-TiO_2 at different methyl parathion concentrations and different temperatures is investigated, and the effect of different methyl parathion concentrations on the degradation activity of OPH@Au-H-TiO_2 is shown in Fig. 6c. As the concentration of methyl parathion increase, the degradation activity of the OPH@Au-H-TiO_2 shows a trend of gradually increasing. The degradation activity is up to 1.3 μmol/min/g when the methyl parathion concentration is 0.5 μmol/mL. Few additional degradation activity are achieved with higher concentration. According to Fig. 6d, at the early stage of the enzymatic reaction, the degradation activity of the OPH@Au-H-TiO_2 increases with the temperature rise due to the fast contact between the substrate and the OPH molecules. When the temperature is 45°C, the enzyme activity reaches the maximum. OPH molecules are easy to stretch at a higher temperature, which results in denaturation from structural change, and loss of the enzyme activity. Thus, the optimal methyl parathion concentration and immobilized temperature are 0.5 μmol/mL and 45°C.

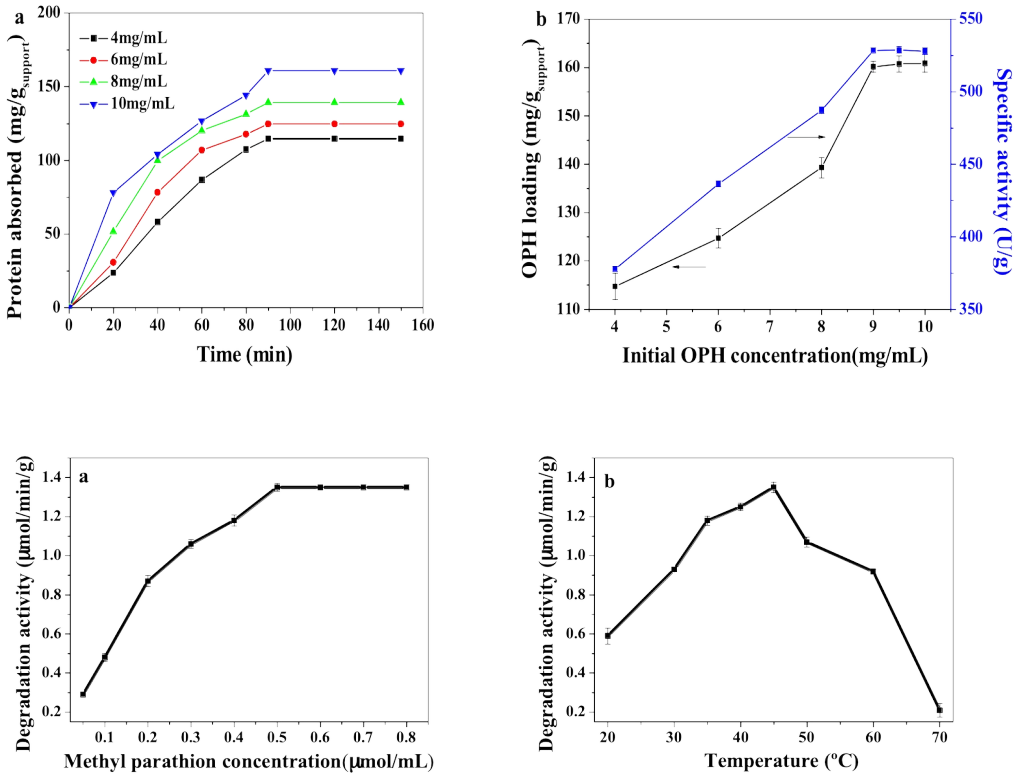

Fig. 6 (a) Immobilization process of OPH with time at different concentrations of enzyme on Au-H-TiO_2, (b) effect of initial OPH concentration on OPH loading amount at 90 min and degradation activity of OPH@Au-H-TiO_2. The catalytic reaction of OPH@Au-H-TiO_2 under different conditions of (c) methyl parathion concentration; (d) degradation activity at different temperature.

3.4 Catalytic performance of OPH@Au-H-TiO_2

In order to research the catalytic performance of OPH@Au-H-TiO_2 in the degradation of methyl parathion under visible light, the degradation of methyl parathion and the relative concentration of p-NP are studied respectively. The results are shown in Fig. 7a and Fig. 7b.

According to the curve of Model 1 in Fig. 7a, the degradation rate of methyl parathion reaches 100% at 30 min. The relative concentrations of p-NP is shown in Fig. 7b. In Model 1, the p-NP concentration increases and then decreases, and about 82.64% of the generated p-NP is degraded after reaction for 2.5 h. As seen in the

curve of Model 2 in Fig. 7a, 100% of methyl parathion is hydrolyzed after 40 min, and about 74.76% of the generated p-NP is degraded after reaction for 2.5 h. Therefore, it can be concluded that the reaction of Model 1 is superior to that of Model 2 in terms of the catalytic performance of OPH@Au-H-TiO_2.

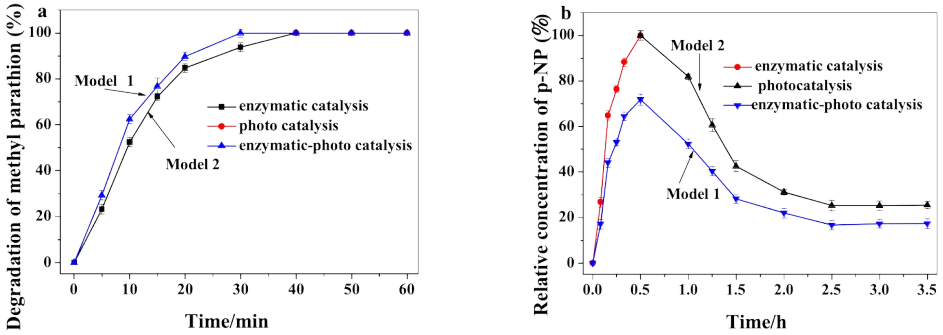

Fig. 7 Catalytic performance of OPH@Au-H-TiO_2 under visible light (λ > 420 nm) degradation of methyl parathion (a); relative concentration of p-NP (b).

3.5 Degradation mechanism of organophosphorus pesticides by OPH@Au-H-TiO_2

In general, superoxide radical ($\bullet O_2^-$), •OH and hole (h^+) are three kinds of free radicals that can effectively degrade organic pollutants. To further understand the degradation mechanism in this experiment, isopropanol (IPA), ethylenediamine tetraacetic acid disodium salt (EDTA-2Na) and benzoquinone (BQ) are used as free radical scavenging substances to study their effect on •OH, $\bullet O_2^-$ and h^+ respectively. The effects of different active substances on the photodegradation rate of P-NP were studied experimentally. From Fig. 8, when 1 mM of IPA was added to the OPH@Au-H-TiO_2 system, the relative concentration of p-NP did not change significantly compared with the control experiment without the addition of free radical scavenging agent, indicating that the effect of •OH on the degradation process is almost

negligible. However, the degradation of p-NP is strongly inhibited when 1 mM of BQ was added, indicating that the $\bullet O_2^-$ plays a major role in the degradation of p-NP by OPH@Au-H-TiO_2. After EDTA-2Na was added to the solution, the degradation rate of p-NP decreases, showing that h^+ is a main role in the degradation of p-NP. Therefore, the experimental results show that $\bullet O_2^-$ is the main active intermediate for OPH@Au-H-TiO_2 to degrade p-NP.

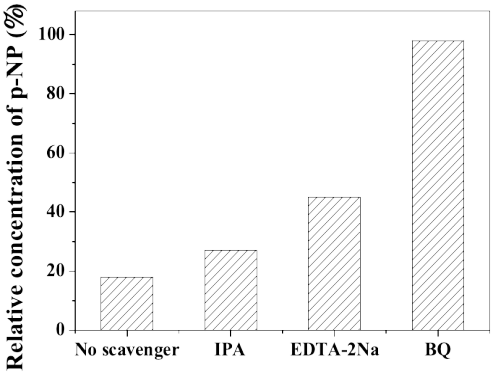

Fig. 8 Effect of different scavengers on the p-NP degradation by OPH@Au-H-TiO_2.

According to the above results, the degradation mechanism of the methyl parathion by OPH@Au-H-TiO_2 can be proposed. As shown in Fig. 9, the P-S bond of methyl parathion is broken under the hydrolysis of OPH enzyme, and the hydrolyzed products include the low-toxic p-NP. When the surface of OPH@Au-H-TiO_2 is irradiated, Au and H-TiO_2 are activated to generate photogenerated electron hole pairs. The generated electron can be transferred from the conduction band (CB) of H-TiO_2 to the CB of Au. Au nanoparticles can prevent the photogenerated electrons from immediately recombining with the holes by receiving the electrons transferred from the CB of TiO_2. At the same time, after activated by SPR effect under light, the Au nanoparticles can transfer the electron to the CB of TiO_2 to achieve rapid electrons

transfer. The electrons can also transfer to the oxygen molecules attached to the OPH@Au-H-TiO_2 surface and thus form more $•O_2^-$. Furthermore, the •OH is generated by the OH^- oxidization-absorbed by h^+. Among them, $•O_2^-$ can degrade p-NP to hydroquinone. By loading Au on H-TiO_2, Au nanoparticles are transferred between the local surface plasma area and the band, which forms a discoupling effect. In addition, the lifetime of local surface plasma is extended, which is beneficial to the electrons transfer [42-44].

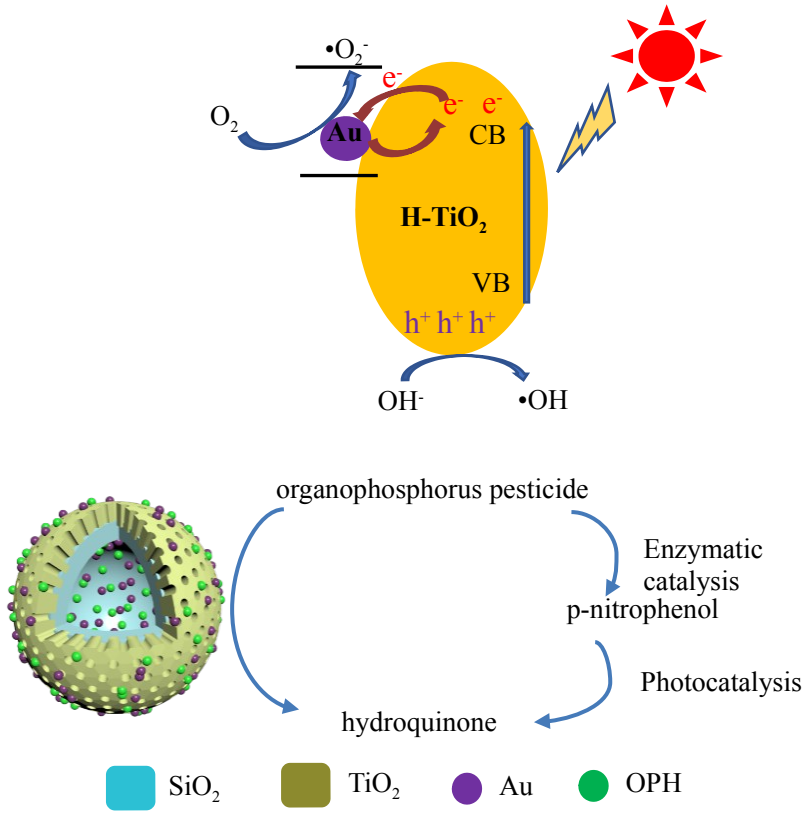

Fig. 9 Proposed photo-enzyme catalysed mechanism of OPH@Au-H-TiO_2 under visible light irradiation.

3.6 The reusability of OPH@Au-H-TiO_2

Fig. 10 shows the reusability of OPH@Au-H-TiO_2 in degradation of methyl parathion. The initial catalytic degradation of methyl parathion is treated as 100%. After reused for 4 times, the degradation activity of OPH@Au-H-TiO_2 for methyl

parathion retains more than 75% in Model 1 and 80% in Model 2. It can be concluded that the retention activity of the stepwise reaction in Model 2 is better than the one-step reaction in Model 1. In the one-step reaction, free radicals produced by photocatalyst can inhibit the activity of OPH, and after reused for 4 times, the activity of OPH is greatly reduced, leading to a decline in the degradation of methyl parathion. On the contrary, in a stepwise reaction (Model 2), such phenomenon can be avoided to retain the activity of OPH. After four cycles, the degradation activity is higher than that of the one-step reaction.

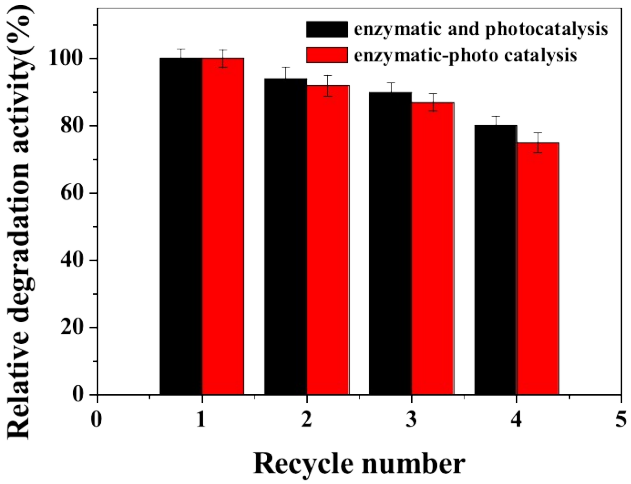

Fig. 10 Reusability of the OPH@Au-H-TiO_2 on degradation of methyl parathion.

4 Conclusions

In conclusion, porous hollow H-TiO_2 microsphere was prepared using SiO_2 nanoflowers as template. The existence of Ti-O-Si bonds in H-TiO_2 can inhibit TiO_2 nucleation, thus stabilizing anatase crystal phase and conducive to photocatalytic efficiency. By loading Au nanoparticles on the H-TiO_2 microspheres, the photocatalyst Au-H-TiO_2 can be obtained. The formation of heterojunction structure

realized the band gap width of TiO_2 from 3.2 eV to 2.68 eV, thus realized the effective use of visible light. Based on the Au-H-TiO_2, the photo-enzyme integrated nanocatalyst OPH@Au-H-TiO_2 was prepared by immobilizing OPH on Au-H-TiO_2. The large specific surface area and good biocompatibility of Au-H-TiO_2 can protect OPH molecules well and reduce the loss of enzyme activity. The photo-enzyme integrated nanocatalyst that combined two catalytic methods can be applied in cascade degradation of methyl parathion under visible light with high catalytic efficiency and reusability. This research provides an effective way for the integration of different catalytic methods.

CONFLICT OF INTEREST

The authors declare no competing financial interest.

ACKNOWLEDGMENTS

This work was supported by the National Natural Science Foundation of China [No. 21576068, 21878066 and 21878068]; the Natural Science Foundation of Hebei Province [B2015202082 and B2017202056]; the Program for Top 100 Innovative Talents in Colleges and Universities of Hebei Province [SLRC2017029] and Hebei High Level Personnel of Support Program [A2016002027]; National College Student's Science and Technology Innovation Project [202010080038].

REFERENCES

1. Kumar, S.; Kaushik, G.; Dar, M. A.; Nimesh, S.; LÓPez-Chuken, U. J.; Villarreal-Chiu, J. F., Microbial degradation of organophosphate pesticides: A review.

Pedosphere 2018, *28* (2), 190-208.

2. Singh, V. V., Recent advances in electrochemical sensors for detecting weapons of mass destruction. A review. *Electroanalysis* 2016, *28* (5), 920-935.

3. Li, J.; Li, H.; Yuan, Z.; Fang, J.; Chang, L.; Zhang, H.; Li, C., Role of sulfonation in lignin-based material for adsorption removal of cationic dyes. *Int. J. Biol. Macromol.* 2019, *135*, 1171-1181.

4. John Victor Peter; John, G., Management of acute organophosphorus pesticide poisoning. *The Lancet* 2008, *371* (9631), 2170.

5. S. Karthikeyan; C. Judia Magthalin; A. B. Mandal; Sekaran, G., Controlled synthesis and characterization of electron rich iron(III) oxide doped nanoporous activated carbon for the catalytic oxidation of aqueous ortho phenylene diamine. *RSC Adv.* 2014, *4*, 19183–19195.

6. Konstantinou; K, I.; Albanis; A, T., TiO_2-assisted photocatalytic degradation of azo dyes in aqueous solution: kinetic and mechanistic investigations: A review. *Appl. Catal. B: Environ.* 2004, *49* (1), 1-14.

7. Yu, J. J.; Wang, T. H.; Rtimi, S., Magnetically separable TiO_2/FeOx/POM accelerating the photocatalytic removal of the emerging endocrine disruptor: 2,4-dichlorophenol. *Appl. Catal. B-Environ.* 2019, *254*, 66-75.

8. Zada, A.; Qu, Y.; Ali, S.; Sun, N.; Lu, H.; Yan, R.; Zhang, X.; Jing, L., Improved visible-light activities for degrading pollutants on TiO_2/g-C_3N_4 nanocomposites by decorating SPR Au nanoparticles and 2,4-dichlorophenol decomposition path. *J Hazard. Mater.* 2018, *342*, 715-723.

9. Ruan, L.; Wang, X.; Wang, T.; Ren, Z.; Chen, Y.; Zhao, R.; Zhou, D.; Fu, G.; Li, S.; Gao, L.; Lu, Y.; Wang, Z.; Tian, H.; Kong, X.; Han, G., Surface defect-controlled growth and high photocatalytic H_2 production efficiency of anatase TiO_2 nanosheets. *ACS Appl. Mater. Inter.* 2019, *11* (40), 37256-37262.

10. Baozhu Tian; Rongfang Dong; Jingming Zhang; Shenyuan Bao; Yang, F., Sandwich-structured AgCl@Ag@TiO_2 with excellent visible-light photocatalytic activity for organic pollutant degradation and E. coli \{K12\} inactivation. *Appl. Catal. B: Environ.* 2014, *158-159*, 76-84.

11. Lu, J.; Lan, L.; Liu, X. T.; Wang, N.; Fan, X., Plasmonic Au nanoparticles supported on both sides of TiO_2 hollow spheres for maximising photocatalytic activity under visible light. *Front. Chem. Sci. Eng.* 2019, *13* (4), 665-671.

12. Yang, X.; Fu, H.; Wang, W.; Xiong, S.; Han, D.; Deng, Z.; An, X., Enhanced solar light photocatalytic performance based on a novel Au-WO_3@TiO_2 ternary core–shell nanostructures. *Appl. Surf. Sci.* 2020, *505*.

13. Yan, X.-Y.; Jiang, Y.-J.; Zhang, S.-P.; Gao, J.; Zhang, Y.-F., Dual-functional OPH-immobilized polyamide nanofibrous membrane for effective organophosphorus toxic agents protection. *Biochem. Eng. J.* 2015, *98*, 47-55.

14. Li, G.; Ma, P.; He, Y.; Zhang, Y.; Luo, Y.; Zhang, C.; Fan, H., Enzyme-nanowire mesocrystal hybrid materials with an extremely high biocatalytic activity. *Nano Lett.* 2018, *18* (9), 5919-5926.

15. Yan, X. Y.; Jiang, Y. J.; Zhang, S. P.; Gao, J.; Zhang, Y. F., Dual-functional OPH-immobilized polyamide nanofibrous membrane for effective organophosphorus toxic

546 agents protection. *Biochem. Eng. J.* 2015, *98* (15), 47-55.
547 16. Tanabe, K.; Sumiyoshi, T.; Shibata, K.; Kiyoura, T.; Kitagawa, J., A new
548 hypothesis regarding the surface acidity of binary metal oxides. *Bulletin of the*
549 *Chemical Society of Japan* 1974, *47* (5), 1064-1066.
550 17. Kibombo, H. S.; Peng, R.; Rasalingam, S.; Koodali, R. T., Versatility of
551 heterogeneous photocatalysis: synthetic methodologies epitomizing the role of silica
552 support in TiO_2 based mixed oxides. *Catal. Sci. Technol.* 2012, *2* (9), 1737-1766.
553 18. Qi, K.; Chen, X.; Liu, Y.; Xin, J. H.; Mak, C. L.; Daoud, W. A., Facile preparation
554 of anatase/SiO_2 spherical nanocomposites and their application in self-cleaning
555 textiles. *J. Mater. Chem.* 2007, *17* (33), 3504-3508.
556 19. Gao, J.; Kong, W.; Zhou, L.; He, Y.; Ma, L.; Wang, Y.; Yin, L.; Jiang, Y.,
557 Monodisperse core-shell magnetic organosilica nanoflowers with radial wrinkle for
558 lipase immobilization. *Chem. Eng. J.* 2017, *309*, 70-79.
559 20. Wu, Y.; Wang, H.; Tu, W.; Liu, Y.; Wu, S.; Tan, Y. Z.; Chew, J. W., Construction
560 of hierarchical 2D-2D $Zn_3In_2S_6$/fluorinated polymeric carbon nitride nanosheets
561 photocatalyst for boosting photocatalytic degradation and hydrogen production
562 performance. *Appl. Catal. B-Environ.* 2018, *233*.
563 21. Bayal, N.; Singh, R.; Polshettiwar, V., Nanostructured silica–titania hybrid using
564 dendritic fibrous nanosilica as a photocatalyst. *ChemSusChem* 2017, *10* (10), 2182-
565 2191.
566 22. Du, D.; Shi, W.; Wang, L.; Zhang, J., Yolk-shell structured Fe_3O_4@void@TiO_2 as
567 a photo-Fenton-like catalyst for the extremely efficient elimination of tetracycline.

568 *Appl. Catal. B: Environ.* 2017, *200*, 484-492.
569 23. Du, X.; He, J., Spherical silica micro/nanomaterials with hierarchical structures:
570 Synthesis and applications. *Nanoscale* 2011, *3* (10), 3984-4002.
571 24. Zhang, W.; He, H.; Tian, Y.; Lan, K.; Liu, Q.; Wang, C.; Liu, Y.; Elzatahry, A.;
572 Che, R.; Li, W.; Zhao, D., Synthesis of uniform ordered mesoporous TiO_2
573 microspheres with controllable phase junctions for efficient solar water splitting.
574 *Chem. Sci.* 2019, *10* (6), 1664-1670.
575 25. And, C. A.; Bard, A. J., Improved photocatalytic activity and characterization of
576 mixed TiO_2/SiO_2 and TiO_2/Al_2O_3 materials. *J. Phy. Chem. B* 1997, *101* (14), 2611-
577 2616.
578 26. Lerdprom, W.; Bhowmik, A.; Grasso, S.; Zapata-Solvas, E.; Jayaseelan, D. D.;
579 Reece, M. J.; Lee, W. E., Impact of spark plasma sintering (SPS) on mullite formation
580 in porcelains. *The Amercian ceramic society* 2017, *101* (2), 525-535.
581 27. Yang, C.; Yao, Y.; Lian, Y.; Chen, Y.; Shah, R.; Zhao, X.; Chen, M.; Peng, Y.;
582 Deng, Z., A double-buffering strategy to boost the lithium storage of botryoid MnOx/
583 C anodes. *Small* 2019, *15* (16), 1900015.
584 28. Dong, G.; Chen, B.; Xiao, X.; Chai, G.; Liang, Q.; Peng, M.; Qiu, J., Morphology
585 and phase control of fluorides nanocrystals activated by lanthanides with two-model
586 luminescence properties. *Nanoscale* 2012, *4* (15), 4658-4666.
587 29. Singh, J.; Sahu, K.; Satpati, B.; Shah, J.; Mohapatra, S., Facile synthesis,
588 structural and optical properties of Au-TiO_2 plasmonic nanohybrids for photocatalytic
589 applications. *J. Phys. Chem. of Solids* 2019, *135*, 109100.

30. Kruk, M.; Jaroniec, M., Gas adsorption characterization of ordered organic-inorganic nanocomposite materials. *Chem. Mater.* 2011, *13*, 3169-3183.

31. Gao, X.; Wang, X.; Yang, Z.; Shen, Y.; Xie, A., A novel bi-functional SiO_2@TiO_2/CDs nanocomposite with yolk-shell structure as both efficient SERS substrate and photocatalyst. *Appl. Surf. Sci.* 2019, *475* (MAY 1), 135-142.

32. He, Q.; Sun, H.; Shang, Y.; Tang, Y.; She, P.; Zeng, S.; Xu, K.; Lu, G.; Liang, S.; Yin, S., Au@TiO_2 yolk-shell nanostructures for enhanced performance in both photoelectric and photocatalytic solar conversion. *Appl. Surf. Sci.* 2018, *441* (MAY31), 458-465.

33. Alamelu, K.; Jaffar, A. B. M., TiO_2-Pt composite photocatalyst for photodegradation and chemical reduction of recalcitrant organic pollutants. *J. Environ. Chem. Eng.* 2018, *6* (5), 5720-5731.

34. Dobrowolska, P.; Krajewska, A.; Gajda-Rączka, M.; Bartosewicz, B.; Nyga, P.; Jankiewicz, B. J., Application of turkevich method for gold nanoparticles synthesis to fabrication of SiO_2@Au and TiO_2@Au core-shell nanostructures. *Materials (Basel)* 2015, *8* (6), 2849-2862.

35. Cho, Y.; Kim, S.; Park, B.; Lee, C. L.; Kim, J. K.; Lee, K. S.; Choi, I. Y.; Kim, J. K.; Zhang, K.; Oh, S. H.; Park, J. H., Multiple heterojunction in single titanium dioxide nanoparticles for novel metal-free photocatalysis. *Nano Lett.* 2018, *18* (7), 4257-4262.

36. Pedrosa, V. A.; Paliwal, S.; Balasubramanian, S.; Nepal, D.; Davis, V.; Wild, J.; Ramanculov, E.; Simonian, A., Enhanced stability of enzyme organophosphate

612 hydrolase interfaced on the carbon nanotubes. *Colloids Surf. B Biointerfaces* 2010, *77*
613 (1), 69-74.
614 37. Fatimah, I.; Prakoso, N. I.; Sahroni, I.; Musawwa, M. M.; Sim, Y.-L.; Kooli, F.;
615 Muraza, O., Physicochemical characteristics and photocatalytic performance of TiO_2/
616 SiO_2 catalyst synthesized using biogenic silica from bamboo leaves. *Heliyon* 2019, *5*
617 (11), e02766.
618 38. Das, A.; Dagar, P.; Kumar, S.; Ganguli, A. K., Effect of Au nanoparticle loading
619 on the photo-electrochemical response of Au–P25–TiO_2 catalysts. *J. Solid State Chem.*
620 2020, *281*, 121051.
621 39. Bai, S.; Zhang, N.; Gao, C.; Xiong, Y. J., Defect engineering in photocatalytic
622 materials. *Nano Energy* 2018, *53*, 296-336.
623 40. Wan, H.; Yao, W.; Zhu, W.; Tang, Y.; Ge, H.; Shi, X.; Duan, T., Fe-N co-doped
624 SiO_2@TiO_2 yolk-shell hollow nanospheres with enhanced visible light photocatalytic
625 degradation. *Appl. Surf. Sci.* 2018, *444*, 355-363.
626 41. Wang, Y.; Yang, C.; Chen, A.; Pu, W.; Gong, J., Influence of yolk-shell Au@TiO_2
627 structure induced photocatalytic activity towards gaseous pollutant degradation under
628 visible light. *Appl. Catal. B: Environ.* 2019, *251*, 57-65.
629 42. Zhang, L.; Qi, H.; Zhao, Y.; Zhong, L.; Zhang, Y.; Wang, Y.; Xue, J.; Li, Y., Au
630 nanoparticle modified three-dimensional network PVA/RGO/TiO_2 composite for
631 enhancing visible light photocatalytic performance. *Appl. Surf. Sci.* 2019, *498*,
632 143855.
633 43. Tsukamoto, D.; Shiraishi, Y.; Sugano, Y.; Ichikawa, S.; Tanaka, S.; Hirai, T., Gold

634 nanoparticles located at the interface of anatase/rutile TiO_2 particles as active
635 plasmonic photocatalysts for aerobic oxidation. *J. Am. Chem. Soc.* 2012, *134* (14),
636 6309-6315.
637 44. Shahini, P.; Ashkarran, A. A., Immobilization of plasmonic Ag-Au NPs on the
638 TiO_2 nanofibers as an efficient visible-light photocatalyst. *Colloids and Surf. A:*
639 *Physicochem. Eng. Aspects* 2018, *537*, 155-162.
640